

# Anti-reflection coatings for highly anisotropic materials in the mid infrared

HONGYAN MEI,<sup>1,†</sup> JIN-WOO CHO,<sup>1,†</sup> JAE-SEON YU<sup>2</sup>, HUANDONG CHEN<sup>3</sup>, SHANTANU SINGH<sup>3,4</sup>, BOYANG ZHAO<sup>3</sup>, JAYAKANTH RAVICHANDRAN<sup>3,4</sup>, SUN-KYUNG KIM<sup>2</sup>, MIKHAIL A. KATS<sup>1,\*</sup>

<sup>1</sup>*Department of Electrical and Computer Engineering, University of Wisconsin-Madison, Madison, WI 53706, USA*

<sup>2</sup>*Department of Applied Physics, Kyung Hee University, Gyeonggi-do 17104, Republic of Korea*

<sup>3</sup>*Mork Family Department of Chemical Engineering and Materials Science, University of Southern California, Los Angeles, CA 90089, USA*

<sup>4</sup>*Core Center for Excellence in NanoImaging, University of Southern California, Los Angeles, CA 90089, USA*

<sup>†</sup>*These authors contributed equally.*

[\\*mkats@wisc.edu](mailto:mkats@wisc.edu)

**Abstract:** We develop and optimize thin anti-reflection coatings (ARCs) for highly anisotropic materials in the mid infrared. Unlike conventional ARCs that assume nearly isotropic refractive indices, this work fully integrates the anisotropic nature of materials into the design process. We describe two designs of thin ARCs for highly anisotropic materials: a single form-birefringent layer, and a planar bilayer. We realized the planar bilayer ARC experimentally, demonstrating excellent mid-infrared anti-reflectance across over a broad range of angles for all polarizations.

## 1. Introduction

Anti-reflection coatings (ARCs) reduce surface reflections and increase light transmission across interfaces in optical systems. While the simplest ARCs for conventional materials and near-normal incidence comprise a single transparent quarter-wave layer with a refractive index that is the geometric mean of the substrate and superstrate<sup>1</sup>, most high-performance ARCs at visible and near-infrared wavelengths use multiple (e.g., 3–15) layers to achieve higher performance or additional functionalities<sup>2–6</sup>.

The multilayer approaches can be used for wavelength ranges beyond the visible and near infrared, but with some practical limitations; for example, in the mid-infrared (mid-IR), there are fewer highly transparent materials that can be readily deposited compared to shorter wavelengths, and each layer must be an order of magnitude thicker due to the longer wavelength. Example mid-IR ARCs that have been recently demonstrated include a four-layer ARC for silicon (Si) using zinc sulfide (ZnS), yttrium fluoride (YF<sub>3</sub>), and germanium (Ge), totaling 2.5 micron and achieving < 1% reflection over the range of 7–12  $\mu\text{m}$ <sup>7</sup>, and a 11-layer coating using YF<sub>3</sub> and ZnS, totaling  $\sim$ 2  $\mu\text{m}$ , and achieving broadband anti-reflectance for 1.5–15  $\mu\text{m}$ <sup>8</sup>.

Our paper tackles the specific challenge of ARCs for highly anisotropic materials in the mid-IR, which comes up when trying to incorporate optical components comprising these anisotropic materials into optical systems. For example, it may be desirable to create an ultrathin mid-IR waveplate from a highly birefringent material, such as one of the A<sub>1+x</sub>BX<sub>3</sub> quasi-1D chalcogenides, BaTiS<sub>3</sub><sup>9–12</sup> and Sr<sub>9/8</sub>TiS<sub>3</sub><sup>13,14</sup>, but this can only be done if reflection for all polarizations is suppressed at the same time.

In  $\text{BaTiS}_3$ , the difference in refractive index ( $\Delta n = n_e - n_o$ ) along different directions can be as large as  $\Delta n > 0.75$ , and in  $\text{Sr}_{9/8}\text{TiS}_3$   $\Delta n$  can exceed 2 [Fig. 1]. This direction-dependent refractive index results in varying Fresnel reflectance and transmittance based on light polarization and propagation direction, complicating ARC design, which is further complicated by the thickness and material limitations in the mid-IR.

Here, we designed two ARC structures to minimize the number of layers while achieving good anti-reflection performance: a single-layer structure that requires lithographic patterning, and a planar bilayer structure that can be vapor-deposited with no lithography. We fabricated the bilayer structure as an ARC for  $\text{BaTiS}_3$ , which demonstrated robust performance over broad infrared spectral ranges and wide incident angles for both ordinary and extraordinary polarization. Our findings offer design guidelines for ARCs tailored for anisotropic materials.

## 2. Theory and calculations

The quasi-one-dimensional materials  $\text{BaTiS}_3$  and  $\text{Sr}_{9/8}\text{TiS}_3$  have some of the largest optical birefringence measured in the mid-IR [Fig. 1], resulting from a combination of anisotropic  $\text{ABX}_3$  structure and picometer-scale atomic displacements in the case of  $\text{BaTiS}_3$ <sup>9,11</sup>, and structural modulations resulting in enhanced anisotropy in the polarizability in the case of  $\text{Sr}_{8/9}\text{TiS}_3$ <sup>13</sup>. In these anisotropic materials, the interface (Fresnel) reflectance has large polarization dependence even at normal incidence [Figs. 1(c, f)].

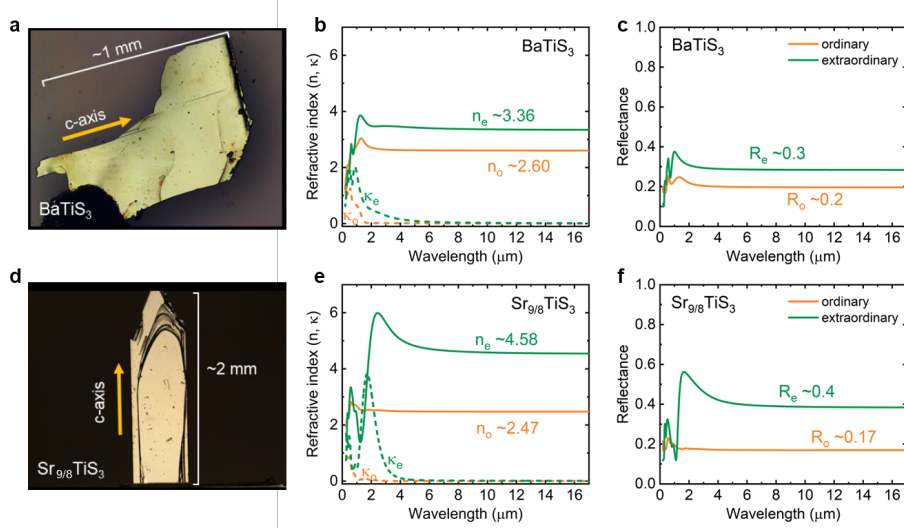


**Figure 1.** (a, d) Optical images of (a) a  $\text{BaTiS}_3$  crystal, and (d) a  $\text{Sr}_{9/8}\text{TiS}_3$  crystal. The  $c$ -axis lies in plane along the direction indicated by the orange arrow. (b, e) Complex refractive indices for (b)  $\text{BaTiS}_3$  and (e)  $\text{Sr}_{9/8}\text{TiS}_3$ , from 210 nm to 17  $\mu\text{m}$ , for light polarized parallel (extraordinary direction,  $n_e$ ) and perpendicular (ordinary direction,  $n_o$ ) to the  $c$ -axis. The  $\text{BaTiS}_3$  panels are adapted from ref.<sup>9</sup>, and the  $\text{Sr}_{9/8}\text{TiS}_3$  panels are adapted from ref.<sup>13</sup>. (c, f) Calculated normal-incidence reflectance at an interface between air and (c)  $\text{BaTiS}_3$  and (f)  $\text{Sr}_{9/8}\text{TiS}_3$ .

### 2.1 Single-layer form-birefringent ARC

The simplest conventional ARC to air is composed of a single thin layer of transparent material, whose refractive index is the square root of the substrate's refractive index, with a thickness equivalent to a quarter of a designated wavelength. For birefringent substrates like  $\text{BaTiS}_3$  and  $\text{Sr}_{9/8}\text{TiS}_3$ , the single layer must meet the “quarter-wave” condition for both the ordinary and

extraordinary axes simultaneously, while maintaining a uniform thickness, which cannot be achieved with isotropic films. Therefore, we designed a form-birefringent<sup>15</sup> anisotropic ARC, comprising subwavelength ridges [Figs. 2(a, d)].

Effective medium theory (EMT) can be used to aid with the design of such form-birefringent structures. For subwavelength ridges with a rectangular cross-section, the parallel and perpendicular effective refractive index can be approximated as<sup>16,17</sup>:

$$\tilde{n}_{\parallel} = [(1 - D)\tilde{n}_1^2 + D\tilde{n}_2^2]^{1/2} \quad (1)$$

$$\tilde{n}_{\perp} = \frac{\tilde{n}_1 \cdot \tilde{n}_2}{[D\tilde{n}_1^2 + (1 - D)\tilde{n}_2^2]^{1/2}} \quad (2)$$

where  $D$  is the duty cycle,  $n_1$  is the index of the matrix (e.g., air), and  $n_2$  is the index of the material comprising the ridges. In our design, we position the ridges in the direction of the  $c$ -axis of the substrate  $\text{ABX}_3$  material [Figs. 2(a, d)].

We first calculate the geometric mean of the indices of the substrate ( $\text{ABX}_3$  material) and superstrate (air) along two different orientations, yielding the required  $n_{\parallel}$  and  $n_{\perp}$  for the ARC. We then plug these into the EMT equations (Eqn. 1 and Eqn. 2), along with  $n_1 = 1$  (air), and solve the two equations simultaneously to get the index of the ideal ridge material,  $n_2$ , and the corresponding duty cycle  $D$ . To meet the quarter-wave ARC condition for both polarizations at normal incidence, we calculate the thickness  $t$  by using the average index  $(n_1 + n_2)/2$ , targeting a wavelength of 10  $\mu\text{m}$ . We then selected a period for the ridges of 2  $\mu\text{m}$ , which is subwavelength but large enough for conventional photolithography. This calculation for  $\text{BaTiS}_3$  at  $\lambda = 10 \mu\text{m}$ , yields  $n_2 \approx 1.96$ ,  $D \approx 0.8$ ,  $t \approx 1.60 \mu\text{m}$ , whereas for  $\text{Sr}_{9/8}\text{TiS}_3$ ,  $n_2 \approx 2.45$ ,  $D \approx 0.71$ ,  $t \approx 1.35 \mu\text{m}$ .

We carefully reviewed possible transparent materials for vapor deposition and identified each material's transparency window, here defined by an absorption coefficient of  $< 10 \text{ cm}^{-1}$ , for material selection in the design, as shown in Fig. 3. Based on the optimum  $n_2$  values obtained from the EMT calculation,  $\text{ZnS}$  ( $n \sim 2.2$ ) and  $\text{ZnSe}$  ( $n \sim 2.4$ ) were chosen to be the most suitable materials to achieve the target  $n_2$  values for  $\text{BaTiS}_3$  and  $\text{Sr}_{9/8}\text{TiS}_3$ , respectively. They exhibit high refractive indices and broad transparency windows across the wavelength range of interest (highlighted area in the Fig. 3a).

To fine-tune our design, we performed full simulations using the finite-difference time-domain (FDTD) method to obtain precise values of the duty cycle and thickness. For  $\text{BaTiS}_3$ , we found a combination of air and  $\text{ZnS}$  with a duty cycle of  $D = 0.725$  and a thickness of  $t = 1.35 \mu\text{m}$  [Figs. 2(a–c)]. For  $\text{Sr}_{9/8}\text{TiS}_3$ , we identified a combination of air and  $\text{ZnSe}$  with a duty cycle of  $D = 0.7$  and a thickness of  $t = 1.25 \mu\text{m}$  [Figs. 2(d–f)].

The resulting ARCs suppress reflectance at  $\lambda = 10 \mu\text{m}$  to  $R < 0.01$ , though notably the reflectance minimum is at a slightly different wavelength for the two polarizations [Fig. 3(c, f)]. If targeting a particular wavelength, this is an effective ARC strategy. As an example, we found that by applying this single-layer ridge structure to both the top and bottom surfaces of a finite-thick (10  $\mu\text{m}$ )  $\text{BaTiS}_3$  and  $\text{Sr}_{9/8}\text{TiS}_3$  crystals, interference-induced Fabry–Pérot fringes can be substantially mitigated at the design wavelength, as shown in Figs. S1 and S2 in Supplementary Information.

We note that anisotropic ARCs similar to ours have previously been explored in a different context, to suppress reflectance for one polarization but not for another one, assuming an isotropic substrate<sup>18</sup>.

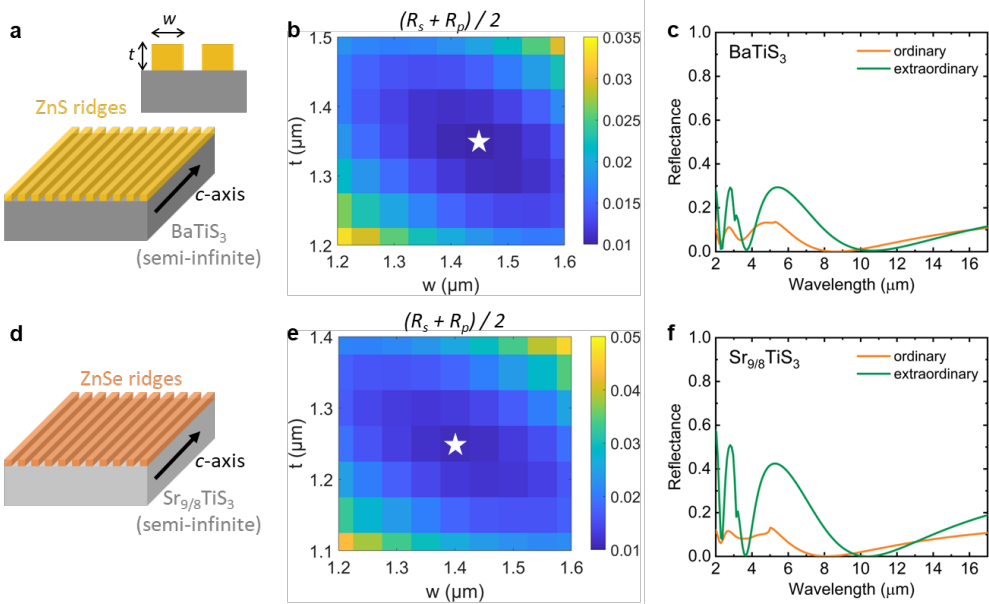


**Figure 2.** Form-birefringent single-layer ARC using ridges comprising an isotropic material. (a) ZnS ridges on a BaTiS<sub>3</sub> substrate, with ridges oriented along the *c*-axis. (b) Calculated polarization-averaged reflectance,  $(R_s + R_p)/2$ , at  $\lambda = 10 \mu\text{m}$  as a function of ridge thickness ( $t$ ) and width ( $w$ ). The minimum average reflectance occurs at  $w = 1.45 \mu\text{m}$  and  $t = 1.35 \mu\text{m}$ , with a period for the ridges of 2  $\mu\text{m}$ . (c) Calculated  $R_s$  and  $R_p$  spectra for the corresponding  $w$  and  $t$  parameters. (d) ZnSe ridges on an Sr<sub>9/8</sub>TiS<sub>3</sub> substrate, with ridges oriented along the *c*-axis. (e) Calculated polarization-averaged reflectance,  $(R_s + R_p)/2$ , at  $\lambda = 10 \mu\text{m}$  as a function of  $t$  and  $w$ . The minimum average reflection occurs at  $w = 1.4 \mu\text{m}$  and  $t = 1.25 \mu\text{m}$ . (f) Calculated  $R_s$  and  $R_p$  spectra for the corresponding  $w$  and  $t$  parameters.

## 2.2 Planar bilayer ARC

To design a single-layer ARC for an isotropic window, two degrees of freedom (i.e., thickness and refractive index) are sufficient to suppress the reflectance at normal incidence. For an anisotropic window or other substrate, additional degrees of freedom are needed. In Section 2.1, we found that adding a third degree of freedom (duty cycle of ridges) is sufficient to suppress the reflectance for both polarizations of a uniaxial material over a certain wavelength range. However, this subwavelength ridge structure requires patterning. We were motivated to identify a planar ARC design that requires no lithographic patterning.

To increase the number of degrees of freedom available in a planar ARC, we can introduce an arbitrary number of additional layers. However, we also want to keep the total thickness small, since mid-IR wavelengths are substantial compared to typical layer thicknesses that can be easily deposited. This leads to a trade-off between the number/total thickness of layers and the effectiveness of the ARC.

We focused on a bilayer structure to demonstrate a design rule for ARCs for anisotropic materials. Figure 3 shows various low- and high-index materials that are transparent in the mid-IR and can be vapor-deposited. For a target wavelength range from 6 to 10  $\mu\text{m}$ , fluorides (CaF<sub>2</sub>, YF<sub>3</sub>, BaF<sub>3</sub>) feature a low refractive index with a broad transparency window, and ZnS, ZnSe, As<sub>2</sub>S<sub>3</sub>, CdTe, amorphous Si (a-Si), and amorphous Ge (a-Ge) are suitable high-index materials with low loss. Out of these, we selected YF<sub>3</sub> as the low-index material and ZnS, ZnSe, a-Si,

and a-Ge as the high-index materials, because we had access to a physical vapor deposition system that accommodated all of these materials.

We selected BaTiS<sub>3</sub> as the highly anisotropic substrate material, and considered a bilayer ARC on the BaTiS<sub>3</sub> surface. For each possible combination of YF<sub>3</sub> with a high- $n$  material (ZnS, ZnSe, a-Si, and a-Ge), we swept through all possible thicknesses of each layer to minimize the normal-incidence reflectance, averaged over the two polarizations, targeting  $\lambda = 6\text{--}10 \mu\text{m}$ . The best design for each combination is shown in Fig. S3 in *Supplementary Information*. Among these, a combination of a 1.41- $\mu\text{m}$ -thick YF<sub>3</sub> layer and a 0.85- $\mu\text{m}$ -thick ZnS layer can reduce the reflectance of BaTiS<sub>3</sub> to < 2% for both polarizations in the range of 6–10  $\mu\text{m}$ , as shown in Fig. 4.

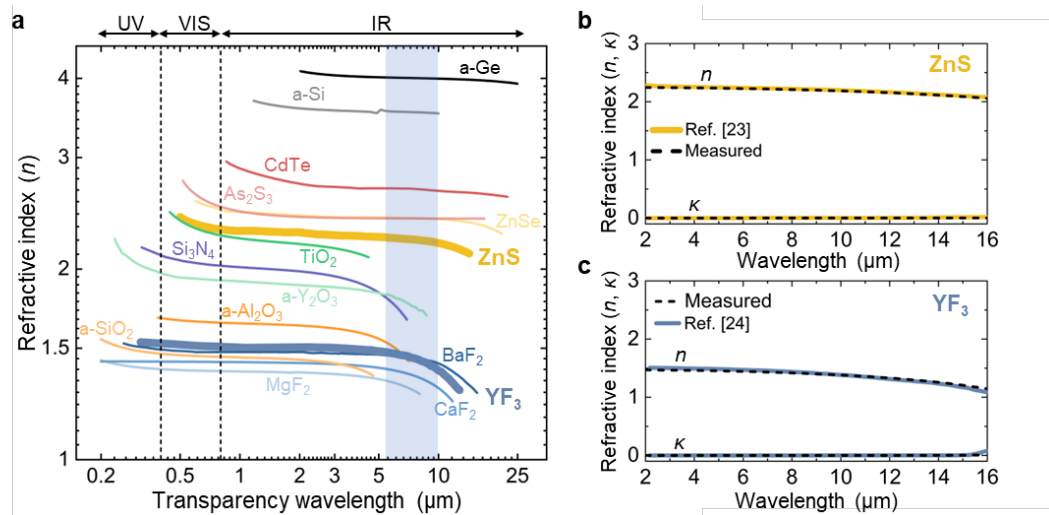


**Figure 3.** Potential low-loss optical materials for mid-IR ARCs. (a) Real part of the refractive index,  $n$ . Curves are plotted only in the wavelength regions where each material has an absorption coefficient  $\alpha < 10 \text{ cm}^{-1}$ . ZnS and YF<sub>3</sub>, which are used for the bilayer ARC in this work, are plotted with thicker lines. All data are from literature (ZnS<sup>19</sup>, YF<sub>3</sub><sup>20</sup>, ZnSe<sup>19</sup>, a-Ge<sup>21</sup>, a-Si<sup>22</sup>, CdTe<sup>23</sup>, As<sub>2</sub>S<sub>3</sub><sup>24</sup>, Si<sub>3</sub>N<sub>4</sub><sup>25</sup>, TiO<sub>2</sub><sup>26</sup>, a-Y<sub>2</sub>O<sub>3</sub><sup>27</sup>, a-Al<sub>2</sub>O<sub>3</sub><sup>26</sup>, a-SiO<sub>2</sub><sup>28</sup>, BaF<sub>2</sub><sup>19</sup>, CaF<sub>2</sub><sup>29</sup>, MgF<sub>2</sub><sup>30</sup>). (b, c) Real ( $n$ ) and imaginary ( $\kappa$ ) parts of the refractive index of e-beam evaporated ZnS and YF<sub>3</sub>, measured using ellipsometry (dashed), compared to the literature data.

The planar bilayer design exhibits good tolerance to variations in film thickness. As shown in Fig. S4 in *Supplementary Information*, varying the YF<sub>3</sub> thickness by  $\pm 200 \text{ nm}$  and the ZnS thickness by  $\pm 150 \text{ nm}$  leads to no significant changes in the reflectance. Additionally, by applying the planar bilayer ARCs to both the top and bottom surfaces of BaTiS<sub>3</sub> crystals, interference induced Fabry-Pérot fringes can be substantially mitigated within the broad design wavelength range (Fig. S5 in *Supplementary Information*).

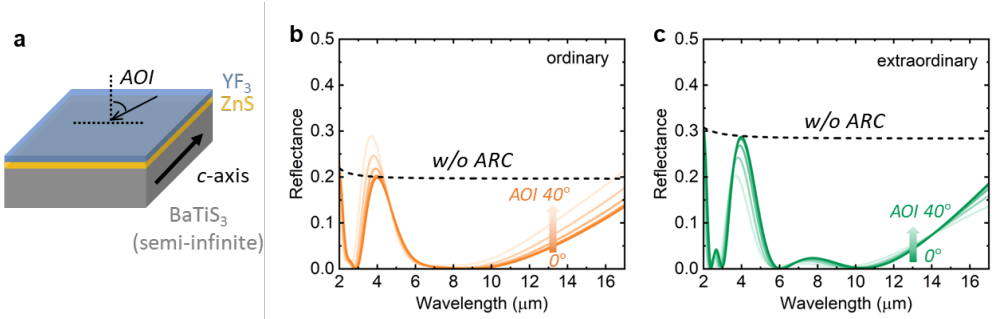


**Figure 4.** (a) Planar bilayer ARC on a BaTiS<sub>3</sub> substrate, with 0.85-μm-thick ZnS and 1.41-μm-thick YF<sub>3</sub>. (b, c) Calculated reflectance at different angles of incidence (AOI) of the structure in (a), showing a small change for angles up to 40° in the range of 6–10 μm.

This simple planar bilayer ARC design also maintains robust performance at oblique incidence, remaining effective for angles exceeding 40°, as shown in Fig. 4 and Fig. S6 in *Supplementary Information*. Such angular insensitivity is particularly important for practical optical systems, where finite numerical aperture, beam divergence, or off-axis illumination inevitably lead to a broad distribution of incidence angles.

Following the same design procedures, we explored planar bilayer ARC designs for Sr<sub>9/8</sub>TiS<sub>3</sub>, and we found that a YF<sub>3</sub>/ZnSe combination provides the best suppression of reflectance for both polarizations (Figs. S7 and S8 in *Supplementary Information*).

### 3. Experimental results

We realized the planar bilayer ARC using electron-beam evaporation of ZnS and YF<sub>3</sub> directly on top of a single crystal of BaTiS<sub>3</sub>. The BaTiS<sub>3</sub> sample is 400 μm wide, ~1 mm long, and 350 μm thick, synthesized via the molten flux growth method<sup>12</sup>, as shown in Fig. 5a.

The BaTiS<sub>3</sub> crystal was mounted on a glass carrier wafer, and loaded into a conventional e-beam evaporator (KVE-E2004, Korea Vacuum Tech.), with depositions performed at 10<sup>-6</sup> Torr (more details in *Methods*). We evaporated 0.85 μm of ZnS directly on the BaTiS<sub>3</sub>, followed by a 10-nm Y<sub>2</sub>O<sub>3</sub> adhesion layer<sup>31</sup>, and then the 1.46-μm-thick YF<sub>3</sub> film. Visually, the YF<sub>3</sub>/ZnS layers appear to be continuous and mostly uniform [Fig. 5d]; the visible fringes indicate relatively small thickness differences across the sample compared to our target mid-IR wavelength. The complex refractive indices of YF<sub>3</sub> and ZnS were obtained by measuring and fitting ~100-nm-thick films of material that were electron-beam evaporated on a quartz wafer using mid-infrared variable-angle spectroscopic ellipsometry (IR VASE, J. A. Woollam), as shown in Figs. 3 (b, c). In our calculation, we also verified that the 10-nm Y<sub>2</sub>O<sub>3</sub> adhesion layer has a negligible effect on the reflectance spectra. We note that while the sample in Fig. 5d is robust, surviving shipment and multiple measurements over many months, some other samples deposited in the same process resulted in delamination.

We measured the reflectance of the same BaTiS<sub>3</sub> crystal with and without the ARC using an infrared microscope using an objective with NA = 0.4, integrated with a Fourier-transform infrared (FTIR) spectrometer. A wire-grid polarizer was used to control the polarization of the incident light, enabling measurement of reflectance along both the ordinary and extraordinary axes.

The measured reflectance spectra of the uncoated BaTiS<sub>3</sub> crystal are shown in Fig. 5b, with reflectance ~0.3 and ~0.2 for the extraordinary and ordinary directions, respectively. The

measurement matches very well with calculations performed using previously published anisotropic complex refractive index data<sup>9,11</sup> [Fig. 5c].

Following deposition of the bilayer ARC, the measured reflectance was substantially suppressed over the 6 to 10  $\mu\text{m}$  range, decreasing from 0.3 to  $\sim 0.007$  for the extraordinary axis and from 0.2 to  $\sim 0.04$  for the ordinary axis [Fig. 5e]. The measurements are in good agreement with the calculations [Figs. 5(c, f)].

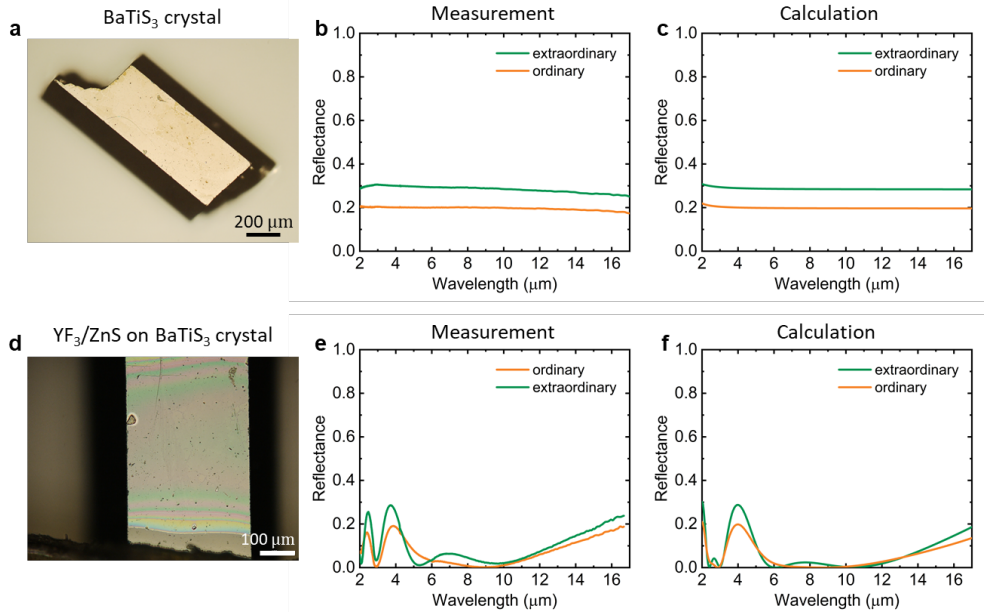


**Figure 5.** BaTiS<sub>3</sub> crystal (a–c) before and (d–f) after deposition of the ARC. (a, d) Optical images of the crystal surface. (b, e) Measured reflectance spectra. (c, f) Calculated reflectance spectra using the transfer-matrix method (TMM), using measured optical properties of BaTiS<sub>3</sub> and of YF<sub>3</sub> and ZnS from Figs. 3(b, c). Note that panel (c) is identical to Fig. 1c and is included here for comparison.

#### 4. Conclusion

This study demonstrates the design and realization of anti-reflection coatings (ARCs) specifically tailored for highly anisotropic materials in the mid-infrared (mid-IR) region, focusing on quasi-one-dimensional ABX<sub>3</sub> crystals BaTiS<sub>3</sub> and Sr<sub>9/8</sub>TiS<sub>3</sub> that have birefringence ( $\Delta n$ ) on the order of unity. Owing to the long wavelengths in the mid-IR, we sought to minimize both the thickness and the number of ARC layers, and accordingly proposed two architectures: (1) a single-layer form-birefringent ARC and (2) a planar bilayer ARC. We experimentally realized the planar bilayer ARC by electron-beam evaporation of yttrium fluoride (YF<sub>3</sub>) and zinc sulfide (ZnS) onto BaTiS<sub>3</sub> and demonstrated substantial suppression of reflectance at this highly anisotropic interface for all polarizations.

The demonstration of ARCs for materials with giant anisotropy will enable the development of optical components such as ultra-thin mid-IR wave plates and polarizers, which would otherwise suffer from strong multiple-interface reflections.

## Methods

### *Single Crystal Growth*

Large single crystals of BaTiS<sub>3</sub> were synthesized using the molten flux method, with potassium iodide (KI) as the flux<sup>12</sup>. First, polycrystalline BaTiS<sub>3</sub> powders were prepared by solid-state reaction at 1040 °C, followed by annealing with excess sulfur (in a 2:1 BaTiS<sub>3</sub>: S weight ratio) at 650 °C. The synthesized BaTiS<sub>3</sub> powders were then mixed with KI in a ~1:100 molar ratio, heated to 1040 °C, and then slowly cooled down to 700 °C (1 °C/h), after which the furnace was turned off. BaTiS<sub>3</sub> crystals were then recovered by washing off the solidified flux with DI water.

### *Thin film deposition*

To analyze the optical and material properties of ZnS (iTasco, 99.99%), YF<sub>3</sub> (iTasco, 99.99%), and Y<sub>2</sub>O<sub>3</sub> (iTasco, 99.99%), ~100-nm-thick thin films of these materials were deposited on a quartz substrate (thickness 500 ± 30 µm, Hi-Solar Co., Ltd.). Before the deposition, the quartz substrates were sequentially cleaned using acetone, isopropyl alcohol, and distilled water with ultrasound, followed by a soft bake at 150 °C for 10 minutes to remove moisture and enhance adhesion.

Before depositing the ARCs, a rapid ICP-RIE was performed to clean the surface of the flux-grown BaTiS<sub>3</sub> samples. To enhance the adhesion of each of the thicker ZnS and YF<sub>3</sub> layers, a 10 nm layer of Y<sub>2</sub>O<sub>3</sub> was deposited before the deposition of each material. The materials mentioned above were sequentially deposited on the samples using a conventional e-beam evaporator (KVE-E2004, Korea Vacuum Tech.) at 10<sup>-6</sup> Torr. The deposition rates were set to 2 Å/sec for the ZnS film, 3 Å/sec for the YF<sub>3</sub> film, and 1 Å/sec for the Y<sub>2</sub>O<sub>3</sub> film. During the deposition process, the substrate temperature was maintained at 150 °C, and a beam source sweep was utilized to ensure stable material deposition.

### *Optical measurement in infrared*

The complex refractive indices of YF<sub>3</sub> and ZnS were obtained by measuring and fitting ~100-nm-thick films of material using mid-IR variable-angle spectroscopic ellipsometry (IR VASE, J. A. Woollam) over a spectral range of 2 to 20 µm at an angle of incidence of 50°, 60°, and 70°. Data analysis and refractive index extraction were performed using WVASE software (J. A. Woollam Co.).

Polarization-resolved infrared spectroscopy was carried out using a Fourier transfer infrared spectrometer (FTIR, Bruker Vertex 70) outfitted with an infrared microscope (Hyperion 2000). A 15× Cassegrain microscope objective with numerical aperture (NA) of 0.4 was used under normal incidence on the (100) face of the BaTiS<sub>3</sub> crystal. These measurements were performed with a Globar source, a potassium bromide (KBr) beam splitter, and a mercury cadmium telluride (MCT) detector. A wire-grid polarizer was used to control the polarization of the incident light. The samples were maintained at room temperature.

## Funding

The work at UW-Madison was supported by ONR, with award no. N00014-20-1-2297.

The work at Kyung Hee University was supported by National Research Foundation of Korea through Nano Material Technology Development Program (2022M3H4A1A02046445).

The crystal growth and characterization, in part, was supported by the Army Research Office (ARO) under award numbers W911NF-21-1-0327 (MURI) and W911NF-24-1-0164 and a US National Science Foundation grant with award number DMR-2122071. The crystal growth and characterization tools in part were supported by an ONR grant with award number N00014-23-1-2818.

## Acknowledgements

H. Mei, J. Cho, and M. A. Kats gratefully acknowledge use of facilities and instrumentation in the UW-Madison Wisconsin Center for Nanoscale Technology ([wcnt.wisc.edu](http://wcnt.wisc.edu)), which is partially supported by the Wisconsin Materials Research Science and Engineering Center (NSF DMR-2309000) and the University of Wisconsin-Madison.

## Disclosures

The authors declare no conflicts of interest.

## Data Availability

The data that support the findings of this study are openly available in Zenodo.

## Supplemental document

See Supplementary Information for supporting content.

## References

1. Yeh, P. *Optical Waves in Layered Media*. (Wiley, 2004).
2. Xi, J.-Q. *et al.* Optical thin-film materials with low refractive index for broadband elimination of Fresnel reflection. *Nat. Photonics* **1**, 176–179 (2007).
3. Schubert, M. F., Poxson, D. J., Mont, F. W., Kim, J. K. & Schubert, E. F. Performance of Antireflection Coatings Consisting of Multiple Discrete Layers and Comparison with Continuously Graded Antireflection Coatings. *Appl. Phys. Express* **3**, 082502 (2010).
4. Raut, H. K., Ganesh, V. A., Nair, A. S. & Ramakrishna, S. Anti-reflective coatings: A critical, in-depth review. *Energy Environ. Sci.* **4**, 3779–3804 (2011).
5. Cole, G. D. *et al.* High-performance near- and mid-infrared crystalline coatings. *Optica* **3**, 647–656 (2016).
6. Shanmugam, N., Pugazhendhi, R., Madurai Elavarasan, R., Kasiviswanathan, P. & Das, N. Anti-Reflective Coating Materials: A Holistic Review from PV Perspective. *Energies* **13**, 2631 (2020).

7. Matsuoka, Y., Mathonneire, S., Peters, S. & Masselink, W. T. Broadband multilayer anti-reflection coating for mid-infrared range from 7  $\mu\text{m}$  to 12  $\mu\text{m}$ . *Appl. Opt.* **57**, 1645–1649 (2018).
8. Lemarquis, F., Begou, T., Moreau, A. & Lumeau, J. Broadband antireflection coatings for visible and infrared ranges. *CEAS Space J.* **11**, 567–578 (2019).
9. Niu, S. *et al.* Giant optical anisotropy in a quasi-one-dimensional crystal. *Nat. Photonics* **12**, 392–396 (2018).
10. Zhao, B. *et al.* Orientation-controlled anisotropy in single crystals of quasi-1D BaTiS<sub>3</sub>. *Chem. Mater.* **34**, 5680–5689 (2022).
11. Zhao, B. *et al.* Giant Modulation of Refractive Index from Picoscale Atomic Displacements. *Adv. Mater.* **36**, 2311559 (2024).
12. Chen, H. *et al.* Molten flux growth of single crystals of quasi-1D hexagonal chalcogenide BaTiS<sub>3</sub>. *J. Mater. Res.* **39**, 1901–1910 (2024).
13. Mei, H. *et al.* Colossal Optical Anisotropy from Atomic-Scale Modulations. *Adv. Mater.* **35**, 2303588 (2023).
14. Mei, H. *et al.* Colossal optical anisotropy from atomic-scale modulations: manuscript data. Zenodo <https://doi.org/10.5281/zenodo.7577670> (2023).
15. Richter, I., Sun, P.-C., Xu, F. & Fainman, Y. Design considerations of form birefringent microstructures. *Appl. Opt.* **34**, 2421–2429 (1995).
16. Lalanne, P. & Lemercier-lalanne, D. On the effective medium theory of subwavelength periodic structures. *J. Mod. Opt.* **43**, 2063–2085 (1996).
17. Rytov, S. M. Electromagnetic Properties of a Finely Stratified Medium. in (2014).
18. Hodgkinson, I. & Wu, Q. H. Anisotropic antireflection coatings: design and fabrication. *Opt. Lett.* **23**, 1553–1555 (1998).
19. Optical Constants of Minerals and Other Materials from the Millimeter to the Ultraviolet. <https://apps.dtic.mil/sti/citations/ADA192210>.
20. Su, W., Li, B., Liu, D. & Zhang, F. The determination of infrared optical constants of rare earth fluorides by classical Lorentz oscillator model. *J. Phys. Appl. Phys.* **40**, 3343 (2007).
21. Burnett, J. H., Benck, E. C., Kaplan, S. G., Stover, E. & Phenis, A. Index of refraction of germanium. *Appl. Opt.* **59**, 3985–3991 (2020).
22. Franta, D., Nečas, D., Zajíčková, L., Ohlídal, I. & Stuchlík, J. Advanced modeling for optical characterization of amorphous hydrogenated silicon films. *Thin Solid Films* **541**, 12–16 (2013).
23. Cadmium Telluride (CdTe). in *Handbook of Optical Constants of Solids* 409–427 (Academic Press, 1997). doi:10.1016/B978-012544415-6.50017-0.
24. Synowicki, R. A. & Tiwald, T. E. Optical properties of bulk c-ZrO<sub>2</sub>, c-MgO and a-As<sub>2</sub>S<sub>3</sub> determined by variable angle spectroscopic ellipsometry. *Thin Solid Films* **455–456**, 248–255 (2004).
25. Luke, K., Okawachi, Y., Lamont, M. R. E., Gaeta, A. L. & Lipson, M. Broadband mid-infrared frequency comb generation in a Si<sub>3</sub>N<sub>4</sub> microresonator. *Opt. Lett.* **40**, 4823–4826 (2015).

26. Franta, D., Nečas, D., Ohlídal, I. & Giglia, A. Dispersion model for optical thin films applicable in wide spectral range. in *Optical Systems Design 2015: Optical Fabrication, Testing, and Metrology V* vol. 9628 342–353 (SPIE, 2015).
27. Yttrium Oxide (Y2O3). in *Handbook of Optical Constants of Solids* 1079–1096 (Academic Press, 1997). doi:10.1016/B978-012544415-6.50096-0.
28. Franta, D., Nečas, D., Ohlídal, I. & Giglia, A. Optical characterization of SiO<sub>2</sub> thin films using universal dispersion model over wide spectral range. in *Optical Micro- and Nanometrology VI* vol. 9890 253–267 (SPIE, 2016).
29. Calcium Fluoride (CaF<sub>2</sub>). in *Handbook of Optical Constants of Solids* 815–835 (Academic Press, 1997). doi:10.1016/B978-012544415-6.50082-0.
30. Franta, D., Nečas, D., Giglia, A., Franta, P. & Ohlídal, I. Universal dispersion model for characterization of optical thin films over wide spectral range: Application to magnesium fluoride. *Appl. Surf. Sci.* **421**, 424–429 (2017).
31. Yu, J.-S. *et al.* Ultrathin Ge-YF<sub>3</sub> antireflective coating with 0.5 % reflectivity on high-index substrate for long-wavelength infrared cameras. *Nanophotonics* **13**, 4067–4078 (2024).

## Supplementary Information

### Anti-reflection coatings for highly anisotropic materials in the mid infrared

HONGYAN MEI,<sup>1,†</sup> JIN-WOO CHO,<sup>1,†</sup> JAE-SEON YU<sup>2</sup>, HUANDONG CHEN<sup>3</sup>, SHANTANU SINGH<sup>3,4</sup>, BOYANG ZHAO<sup>3</sup>, JAYAKANTH RAVICHANDRAN<sup>3,4</sup>, SUN-KYUNG KIM<sup>2</sup>, MIKHAIL A. KATS<sup>1,\*</sup>

<sup>1</sup>Department of Electrical and Computer Engineering, University of Wisconsin-Madison, Madison, WI 53706, USA

<sup>2</sup>Department of Applied Physics, Kyung Hee University, Gyeonggi-do 17104, Republic of Korea

<sup>3</sup>Mork Family Department of Chemical Engineering and Materials Science, University of Southern California, Los Angeles, CA 90089, USA

<sup>4</sup>Core Center for Excellence in NanoImaging, University of Southern California, Los Angeles, CA 90089, USA

<sup>†</sup>These authors contributed equally.

[mkats@wisc.edu](mailto:mkats@wisc.edu)

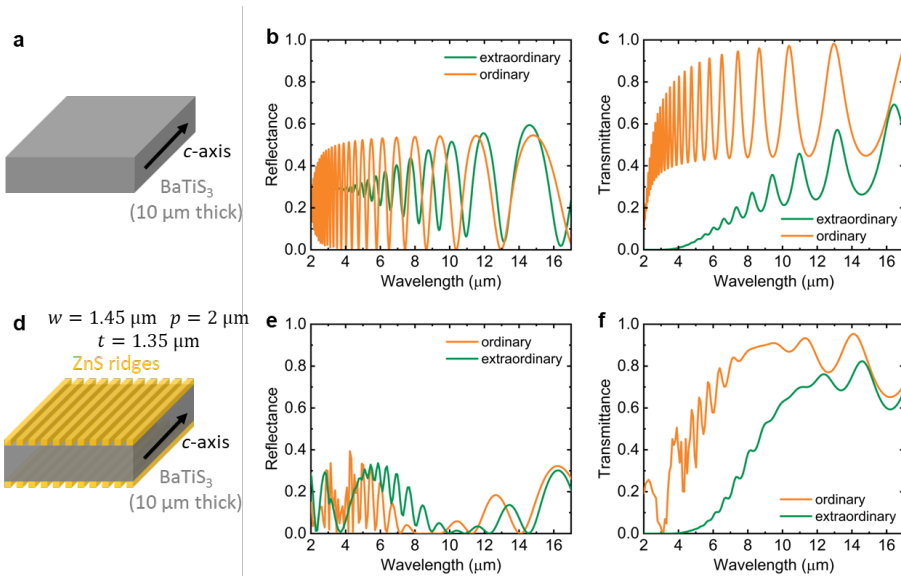


**Figure S1.** (a) Schematic of a 10-μm-thick BaTiS<sub>3</sub> crystal. (b, c) Calculated normal incidence reflectance and transmittance of the structure in (a), showing pronounced Fabry-Pérot fringes. (d) ZnS ridges (1.45 μm width, 2 μm period, 1.35 μm thickness) on both top and bottom surfaces of a 10-μm thick BaTiS<sub>3</sub> crystal, with the ridge direction along the *c*-axis. (e, f) Calculated normal incidence reflectance and transmittance of the structure in (d), showing suppression of reflectance, increase of the transmission, and mitigation of Fabry-Pérot fringes at the designed wavelength  $\lambda = 10$  μm for both polarizations.

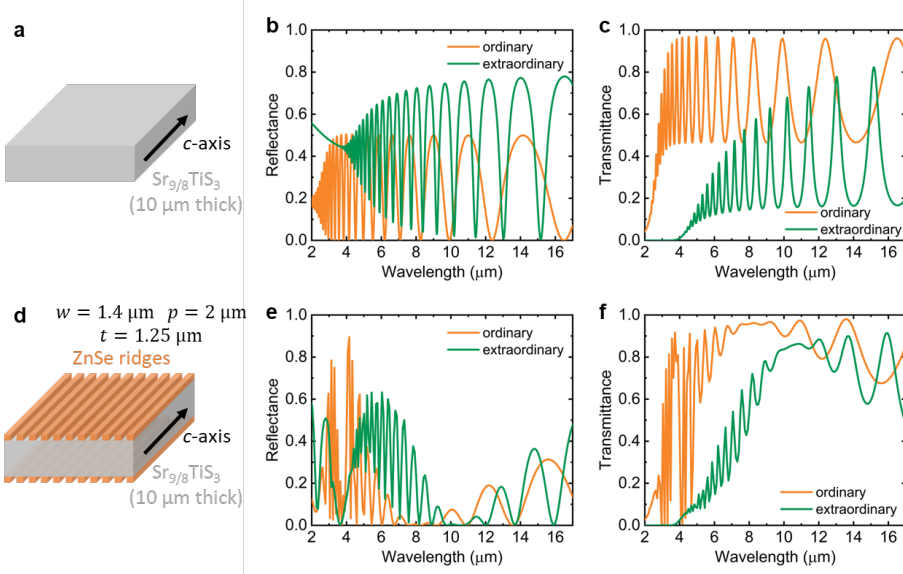


**Figure S2.** (a) Schematic of a 10- $\mu\text{m}$ -thick  $\text{Sr}_{9/8}\text{TiS}_3$  crystal. (b, c) Calculated normal incidence reflectance and transmittance of the structure in (a), showing pronounced Fabry-Pérot fringes. (d) ZnSe ridges (1.4  $\mu\text{m}$  width, 2  $\mu\text{m}$  period, 1.25  $\mu\text{m}$  thickness) on both top and bottom surfaces of a 10- $\mu\text{m}$ -thick  $\text{Sr}_{9/8}\text{TiS}_3$  crystal, with the ridge direction along the  $c$ -axis. (e, f) Calculated normal incidence reflectance and transmittance of the structure in (d), showing suppression of reflectance, increase of the transmission, and mitigation of Fabry-Pérot fringes at the designed wavelength  $\lambda = 10 \mu\text{m}$  for both polarizations.

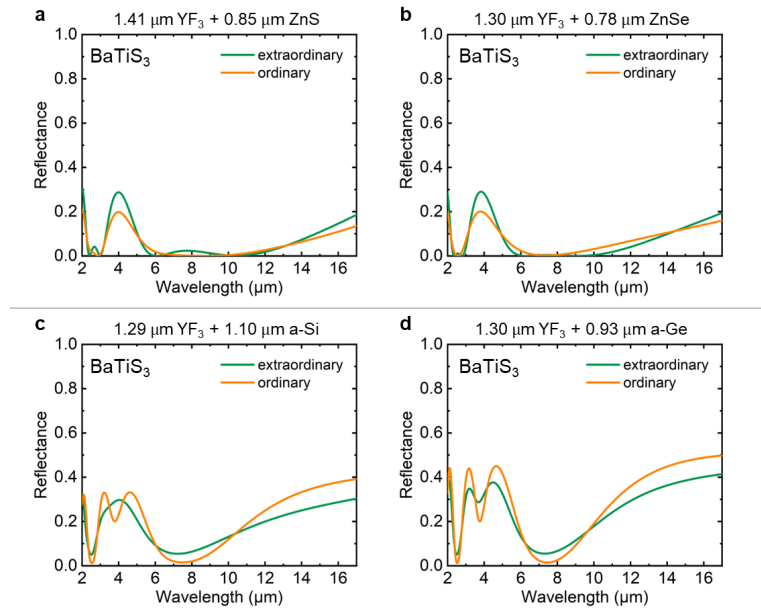


**Figure S3.** Calculated normal incidence reflectance of planar bilayer ARCs on a  $\text{BaTiS}_3$  substrate, with a combination of the low-index material  $\text{YF}_3$  and high-index materials (a) ZnS, (b) ZnSe, (c) a-Si, and (d) a-Ge. The thicknesses of the layers are optimized to minimize the normal-incidence reflectance averaged over the two polarizations, targeting  $\lambda = 6\text{--}10 \mu\text{m}$ .

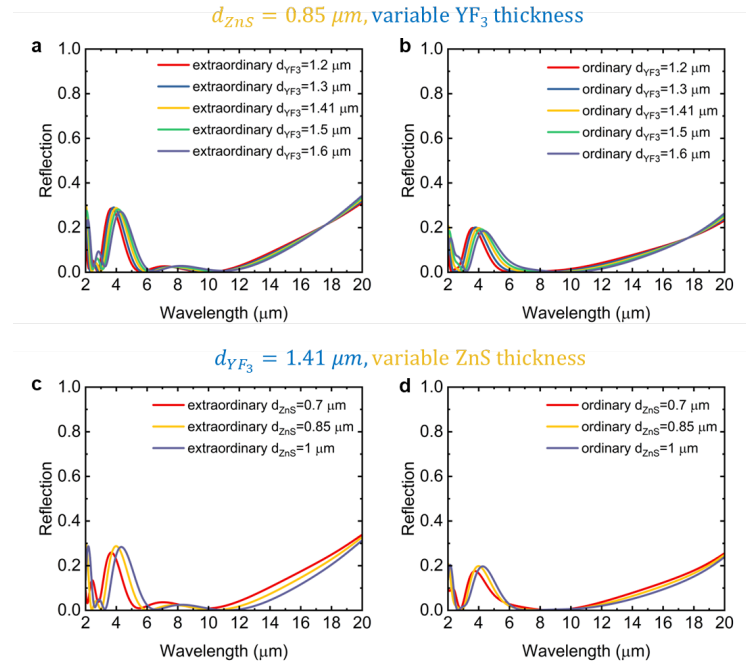


**Figure S4.** Thickness tolerance test for the double-layer  $\text{YF}_3/\text{ZnS}$  ARC for  $\text{BaTiS}_3$ . (a, b) Calculated normal incidence reflectance when varying the thickness of  $\text{YF}_3$  and (c, d) varying the thickness of  $\text{ZnS}$ , showing small changes in reflectance.

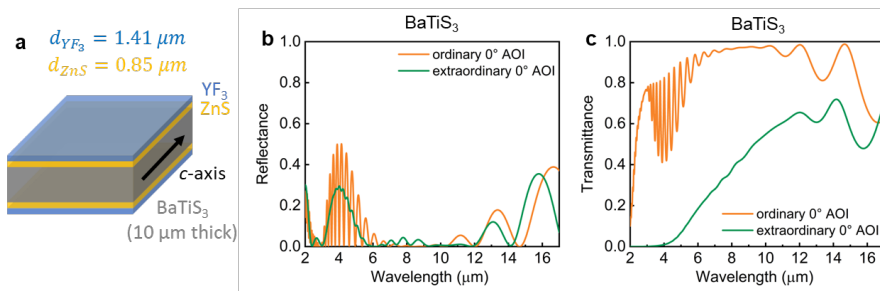


**Figure S5.** (a) Double-layer ARC (1.41- $\mu\text{m}$ -thick  $\text{YF}_3$  + 0.85- $\mu\text{m}$ -thick  $\text{ZnS}$ ) on both top and bottom surfaces of a 10- $\mu\text{m}$ -thick  $\text{BaTiS}_3$  crystal. (b, c) Calculated normal incidence reflectance and transmittance of the structure in (a), showing suppression of reflectance, increase of the transmission, and mitigation of Fabry-Pérot fringes at the designed wavelength range of 6–10  $\mu\text{m}$  for both polarizations. Note that the transmittance and reflectance do not add up to 1 due to optical absorption in  $\text{BaTiS}_3$ .

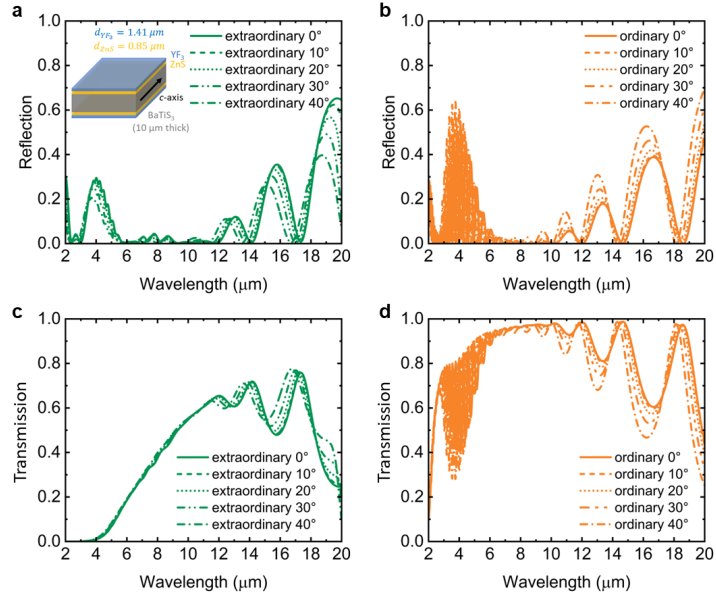


**Figure S6.** (a, b) Calculated reflectance and (c, d) transmittance at different angles of incidence for the structure shown in the inset of (a), showing only small changes for angles up to 40° in the wavelengths of 6–10 μm. The inset in (a) shows a double-layer ARC (1.41-μm-thick YF<sub>3</sub> + 0.85-μm-thick ZnS) on both top and bottom surfaces of a 10-μm-thick BaTiS<sub>3</sub> crystal. Note that the transmittance and reflectance do not add up to 1 due to optical absorption in BaTiS<sub>3</sub>.

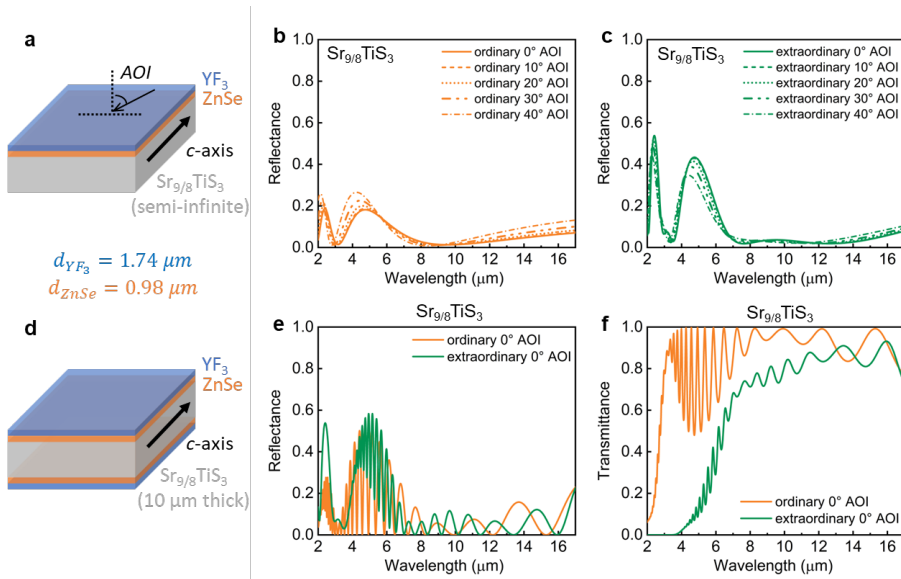


**Figure S7.** (a) Planar bilayer ARC on a Sr<sub>9/8</sub>TiS<sub>3</sub> substrate, with high-index material ZnSe and low-index material YF<sub>3</sub>. (b, c) Calculated reflectance at different angles of incidence of the structure in (a), showing a small change for angles up to 40° in the range of 6–10 μm. (d) Planar bilayer ARC (1.74-μm-thick YF<sub>3</sub> + 0.98-μm-thick ZnSe) on both top and bottom surfaces of a 10-μm-thick Sr<sub>9/8</sub>TiS<sub>3</sub> crystal. (e, f) Calculated reflectance and transmittance of the structure in (a), showing suppression of reflectance, increase of the transmission, and mitigation of Fabry–

Pérot fringes at the designed wavelength range  $\lambda = 6\text{--}10\ \mu\text{m}$  for both polarizations. Note that the transmittance and reflectance do not add up to 1 due to optical absorption in  $\text{Sr}_{9/8}\text{TiS}_3$ .

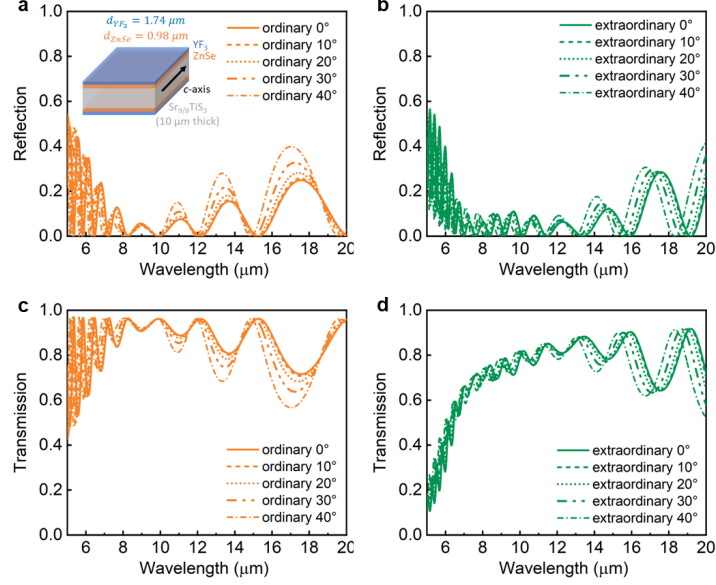


**Figure S8.** (a, b) Calculated reflectance and (c, d) transmittance at different angles of incidence for the structure shown in the inset of (a), showing only small changes for angles up to  $40^\circ$  in the range of 6–10  $\mu\text{m}$ . The inset in (a) shows a double-layer ARC (1.74- $\mu\text{m}$ -thick  $\text{YF}_3$  + 0.98- $\mu\text{m}$ -thick  $\text{ZnSe}$ ) on both top and bottom surfaces of a 10- $\mu\text{m}$ -thick  $\text{Sr}_{9/8}\text{TiS}_3$  crystal. Note that the transmittance and reflectance do not add up to 1 due to optical absorption in  $\text{Sr}_{9/8}\text{TiS}_3$ .